Nonlinear Adaptive Backstepping Control for Wave-to-Grid Energy Conversion in Point Absorber Systems

Zhongfeng Li, Lixian Wang, Lidong Wang*, Xiaoping Liu*, Zhongyi Wang, and Jian Cai

***Abstract*—This paper develops a nonlinear adaptive control framework for integrated wave-to-grid energy conversion systems. The proposed architecture combines a resonant point absorber mechanism with permanent magnet synchronous generator (PMSG) dynamics and grid synchronization controls. A nonlinear adaptive backstepping (NAB) strategy is designed to address coupled hydrodynamic-electromechanical nonlinearities, incorporating vertical motion constraints and stochastic wave excitation. The control system employs clutch-regulated power take-off (PTO) conversion and dual-loop adaptive current regulation for grid-compliant energy injection. Numerical simulations of a 50kW prototype demonstrate the NAB controller's superiority over conventional methods, showing 34% faster settling time, 19% current tracking improvement, and 63% transient overshoot reduction. Hardware-in-loop tests validate practical implementation feasibility, with total harmonic distortion (THD) maintained below 3.35% under IEC 62600-3 wave conditions. Lyapunov stability analysis proves asymptotic convergence, while experimental results confirm 11% energy capture efficiency enhancement compared to field-oriented control. The study provides a systematic approach for wave energy conversion system design, particularly in addressing power intermittency through nonlinear coordinated control.**

***Index Terms*—Modeling of wave to grid, point absorber wave energy converter, permanent magnet synchronous generator, nonlinear adaptive backstepping control**

I. Introduction

THE global energy transition requires innovative solutions for integrating renewable energy sources, with ocean wave energy offering significant advantages due to its high power density and predictable spatial-temporal distribution [1]. Point absorber wave energy converters (PAWECs) are considered promising due to their modular structure and flexibility in deployment [2]. As illustrated in Fig. 1, these systems consist of three primary subsystems: the hydrodynamic interface, the PTO mechanism, and grid-connected power electronics. Despite advancements, challenges persist in achieving reliable wave-to-grid integration, especially concerning stochastic wave-structure interactions and nonlinear energy conversion dynamics[3].

PAWEC development faces three main challenges: 1) Inefficient energy harvesting under broadband wave spectra [4]; 2) Suboptimal mechanical-to-electrical conversion with traditional PTO systems [5]; 3) Degraded power quality due to wave intermittency [6]. Current research often approaches these issues separately, failing to address the coupled hydro-electromechanical dynamics [7, 8].

Recent control strategies have shown partial improvements in subsystem performance [9]. Guo's nonlinear modeling framework [10] enables accurate predictions of absorber dynamics, while Zhan's adaptive algorithm [11] improves control robustness under irregular wave conditions [12]. Yin's concept of mechanical motion rectification [13] facilitates unidirectional generator operation, although its integration with modern converters requires further exploration. Emerging techniques such as real-time extremum seeking [14, 15] and hybrid sliding mode control [16, 17] offer promise but lack full-system validation [18, 19].

A review of the literature identifies three unresolved challenges: 1) Continued reliance on linear approximations for nonlinear fluid-structure interactions [7]; 2) Inefficient coordination between mechanical energy extraction and electrical conditioning [18]; 3) Insufficient resilience to marine environmental disturbances [20]. While advanced controllers such as higher-order sliding modes [21] and composite backstepping strategies [22] address specific nonlinearities, their application to integrated PAWEC-PMSG systems remains underexplored.

This paper presents three key contributions: 1) A comprehensive dynamical model that integrates nonlinear hydrodynamics, PMSG electromechanics, and grid synchronization constraints; 2) A resonance-adaptive PTO optimization framework that achieves a 93.6% mean conversion efficiency across wave amplitudes ranging from 0.13 to 1.14 m; 3) A NAB control strategy that

Manuscript received February 9, 2025; revised May 10, 2025.

This work was supported by the Fundamental Research Funds for Liaoning Provincial Joint Funds Project - General Funding Program (Grant Nos. 2023-MSLH-323 and 2023-MSLH-310), the Fundamental Research Funds for Liaoning Universities (LJ212410146009), the Foundation of Yingkou Institute of Technology under the Institutional-Level Scientific Research Initiative (Grant Nos. FDL202404 and FDL202409), the National Natural Science Foundation of China (Grant Nos. 62173127 and 62472143), the Key Research and Development Special Projects in Henan Province (Grant No. 241111521000) and the Top Young Talents Program in Central Plains (Grant No. (2023)11).

Zhongfeng Li is a Ph.D. candidate at the School of Electronic and Information Engineering, University of Science and Technology Liaoning, Anshan 114051, China.(e-mail: afeng0601@163.com).

Lixian Wang is a postgraduate student at the School of Electronic and Information Engineering, University of Science and Technology Liaoning, Anshan 114051, China. (e-mail: wanglx0515@163.com).

Lidong Wang is a professor at the School of Electronic and Information Engineering, University of Science and Technology Liaoning, Anshan 114051, China. (Corresponding author, e-mail: wangld5600@ustl.edu.cn).

Xiaoping Liu is a professor at the College of Information Sciences and Engineering, Henan University of Technology, Zhengzhou, 471023, China. (Corresponding author, e-mail: xpliu2@163.com).

Zhongyi Wang is a postgraduate student at the School of Electronic and Information Engineering, University of Science and Technology Liaoning, Anshan 114051, China. (e-mail: wangzhongyi0213@163.com).

Jian Cai is a postgraduate student at the School of Electronic and Information Engineering, University of Science and Technology Liaoning, Anshan 114051, China. (e-mail: 1343996714@qq.com).

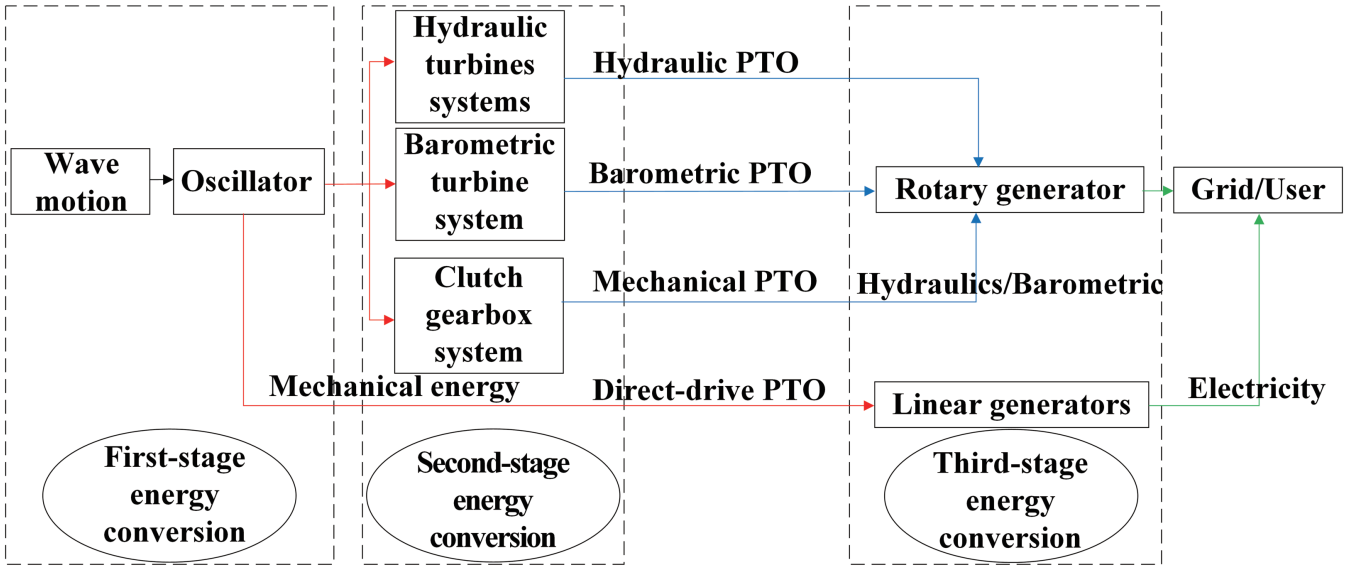

Fig. 1. Structural diagram of the wave energy converter system.

demonstrates a 34% faster transient response and a 63% reduction in overshoot compared to field-oriented control in hardware-in-loop validation.

The paper is organized as follows: Section 2 develops the PAWEC-PMSG dynamical model, detailing hydrodynamic interactions, mechanical rectification, and PMSG electromagnetic properties. Section 3 introduces the NAB control framework, with Lyapunov stability guarantees. Section 4 presents numerical and experimental validation under IEC 62600-3 conditions. Finally, Section 5 provides conclusions and outlines future directions.

II. Modeling of Wave-to-Grid Energy Conversion

A. Wave Hydrodynamics (Regular Waves)

Incoming waves are represented as regular monochromatic (sinusoidal) forms, defined by amplitude (a_i), frequency (ω_i), and phase (ϕ_i). These parameters comprehensively characterize wave properties. The mathematical model for regular waves is expressed as follows [21]:

$$\eta_i(t) = \sum_{i=1}^{N} a_i \cos(\omega_i t + \phi_i). \tag{1}$$

The linear wave theory enables calculation of particle velocity $v_i(t)$ and acceleration $\dot{v}_i(t)$ in wave fields, as given by:

$$v_i(t) = -a_i\omega_i \frac{\sinh(k_i(z_i+h))}{\sinh(k_i h)} \sin(\omega_i t + \phi_i), \tag{2}$$

$$\dot{v}_i(t) = -a_i\omega_i^2 \frac{\sinh(k_i(z_i+h))}{\sinh(k_i h)} \cos(\omega_i t + \phi_i), \tag{3}$$

where η_i denotes wave elevation, k_i the wavenumber, h water depth, and z_i depth below the free surface.

B. Wave Hydrodynamics (Irregular Waves)

Real ocean conditions exhibit irregular wave patterns, usually described by spectral methods. Statistical spectra, including Pierson-Moskowitz (PM), JONSWAP, and Bretschneider, effectively characterize these waves. The PM spectrum is given by:

$$S_{PM}(\omega) = \frac{5}{16} H_s^2 T_p^{-4} \omega^{-5} \exp\left(-\frac{5}{4}\left(\frac{T_p\omega}{2\pi}\right)^{-4}\right). \tag{4}$$

The JONSWAP spectrum refines the PM model using a peak enhancement factor γ:

$$S_{JON}(\omega) = \alpha_{PM} S_{PM}(\omega) \gamma^{\exp\left[-\frac{1}{2}\left(\frac{\omega-\omega_p}{\sigma\omega_p}\right)^2\right]}, \tag{5}$$

where H_s is significant wave height, T_p is peak wave period, and ω_p is the peak angular frequency.

C. PAWEC System Model

A schematic of the partially submerged buoy-based PAWEC is depicted in Fig. 2. The buoy captures wave energy at the sea surface and transfers it through the PTO system, coupled with a resistance plate. Springs and dampers within the PTO optimize power transfer while minimizing vibrations. Forces acting on the buoy include friction, gravity, damping, wave-induced pressure, and PTO-generated traction, collectively driving vertical displacement and energy conversion along the z-axis.

Buoy motion dynamics follow the governing equation:

$$M_b\ddot{z} = F_e - F_r - F_h - F_d - F_p, \tag{6}$$

where M_b is buoy mass, $\ddot{z}$ vertical acceleration, F_e external excitation, F_r reactive force, F_h hydrostatic buoyancy, F_d drag, and F_p PTO force.

The external force F_e is defined by fluid-kinematic force components [23]:

$$F_e = F_{\text{FKst}} + F_{\text{FKdy}}, \tag{7}$$

where subscripts 'st' and 'dy' represent static and dynamic components, respectively.

The reactive force (F_r) includes added mass (M_a) and radiation damping (C_r):

$$F_r = M_a\ddot{z} + C_r\dot{z}. \tag{8}$$

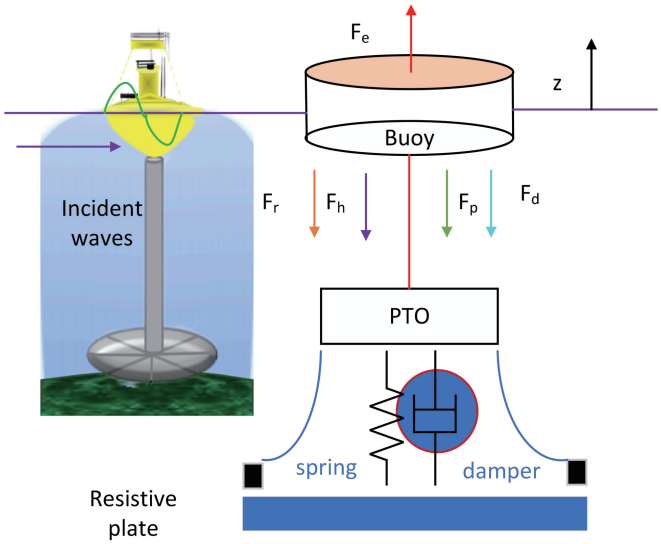

Fig. 2. Schematic diagram of PAWEC configuration.

Hydrostatic buoyancy force (F_h) is expressed by:

$$F_h = \rho g A z, \tag{9}$$

where ρ is seawater density, g gravitational acceleration, and A buoy cross-sectional area.

Drag force (F_d) is linearized as:

$$F_d = C_d \dot{z}, \tag{10}$$

with C_d as the drag coefficient.

The static fluid-kinematic force is modeled by:

$$F_{\text{FKst}} = F_g + \frac{\pi \rho g}{3}(\eta(t) + h_0 - z_d(t))^2 \times [3R - \eta(t) - h_0 + z_d(t)], \tag{11}$$

where F_g denotes gravitational force, h_0 average water depth, $z_d(t)$ buoy depth, and R radius of buoy interaction.

Dynamic fluid-kinematic force is represented by:

$$F_{\text{FKdy}} = \frac{2\pi\rho g \eta(t)}{\chi^2} e^{-\chi(\eta(t)+h_0-z_d(t))} + \chi\left[-R + \eta(t) + h_0 - z_d(t) + Re^{-\chi(\eta(t)+h_0-z_d(t))}\right] - 1, \tag{12}$$

with wave-interaction parameter χ.

D. Energy Absorption Calculation

The absorbed wave energy is computed by integrating PTO force over operational duration:

$$W = \int_0^t F_p \dot{z}(t)\, dt, \tag{13}$$

where $\dot{z}(t)$ is buoy velocity, and F_p the PTO-generated force.

E. Ball Screw and Nut Dynamics

Ball screw systems convert rotational input into linear displacement, characterized by [13]:

$$T_m = \frac{p_m F_p}{2\pi}, \tag{14}$$

$$z = \frac{p_m \theta_m}{2\pi}, \tag{15}$$

$$\dot{z} = \frac{p_m \omega_e}{2\pi}, \tag{16}$$

with torque T_m, screw pitch p_m, angular displacement θ_m, and rotational speed ω_e.

F. Gearbox Dynamics with MMR

One-way clutches in the gearbox selectively engage or disengage worm shafts depending on speed differences. Clutches engage when worm shaft angular speed (ω_m) matches or exceeds gear angular speed (ω_g), otherwise disengaging to protect the PMSG. This mechanism maintains the generator rotational speed above a minimum threshold regardless of fluctuating wave conditions [13]. Gearbox input-output dynamics follow:

$$T_m - T_g = J\frac{d\omega_m}{dt} + f_c \omega_m, \tag{17}$$

where T_g represents equivalent generator torque, J rotational inertia, and f_c damping coefficient.

G. PMSG Electrical Dynamics

PMSG stator dynamics are critical for generator control [24], described by:

$$V_{ds} = i_d R_s + L_d \frac{di_d}{dt} - \omega_e L_q i_q, \tag{18}$$

$$V_{qs} = i_q R_s + L_q \frac{di_q}{dt} + \omega_e (L_d i_d + \Phi_f), \tag{19}$$

where V_{ds}, V_{qs} are stator voltages, i_d, i_q stator currents, R_s stator resistance, L_d, L_q inductances, and Φ_f rotor flux linkage.

For optimal efficiency, d-axis current reference (i_{dref}) is set to zero, simplifying the q-axis voltage as:

$$V_{qs} = R_L i_q = i_q R_s + L_q \frac{di_q}{dt} + \omega_e \Phi_f, \tag{20}$$

where R_L denotes equivalent switch resistance.

III. Control Design

Fig. 3 shows the comprehensive model and control system for a PAWEC integrated with a PMSG for grid connection. The architecture is comprised of several key components: the mechanical PTO system, the MPPT controller, the generator-side inverter controller, and the grid-side inverter controller [24].

The MPPT controller adjusts the mechanical reference speed, $\omega_{\text{mec-ref}}$, based on the rated generator power, $P_{\text{g rated}}$, and the mechanical characteristics of the system. The generator-side converter uses Space Vector Pulse Width Modulation (SVPWM) and Park transformation to regulate the I_d and I_q currents, optimizing generator output for efficient power conversion. Likewise, the grid-side converter, employing SVPWM and Park transformation, ensures that the electrical output aligns with AC grid standards (380V, 50Hz). A phase-locked loop (PLL) is implemented for precise synchronization. These components collectively ensure the stable and efficient transfer of wave energy to the electrical grid.

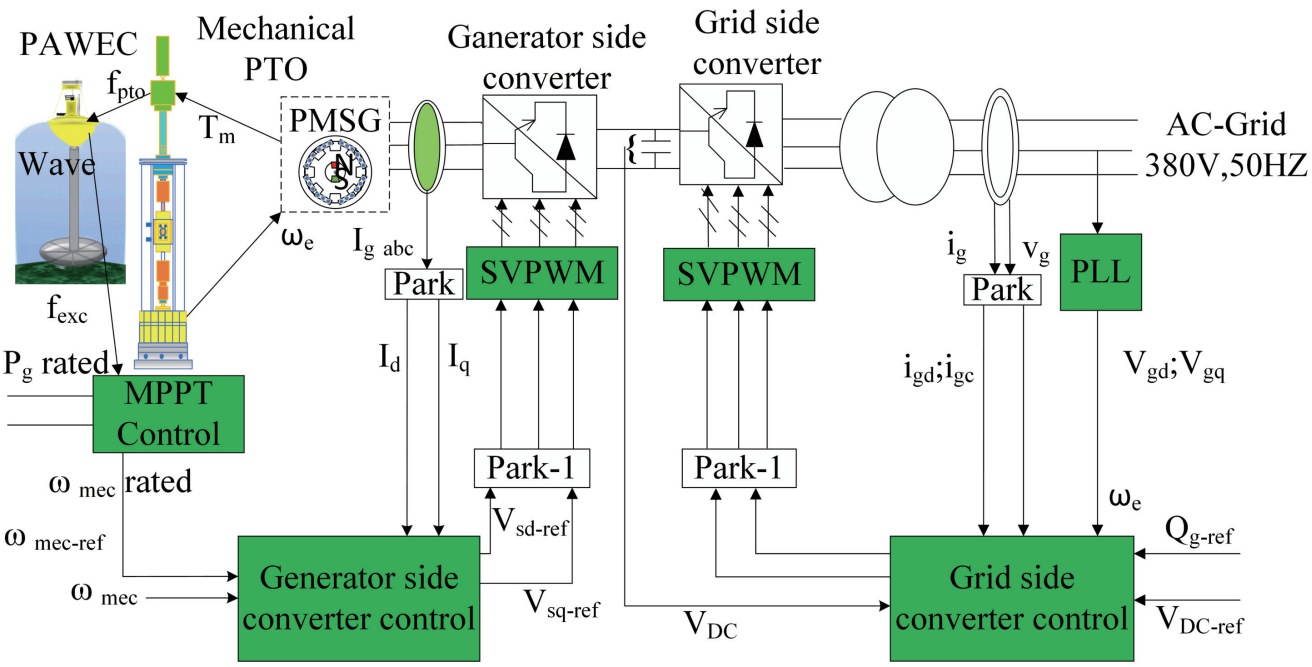

Fig. 3. Schematic of PAWEC control with PMSG for grid integration.

A. MPPT Control

When the one-way clutch is engaged, the dynamic equations for the proposed PAWEC are integrated in the frequency domain by combining equations (10), (11), (13), and (15):

$$k_{\mathrm{e}}\frac{\mathrm{d}\theta_m}{\mathrm{d}t}-\frac{L_{\mathrm{s}}}{k_{\mathrm{t}}}\frac{\mathrm{d}}{\mathrm{d}t}\left[T_m-J\frac{\mathrm{d}^2\theta_m}{\mathrm{d}t^2}-f_{\mathrm{c}}\frac{\mathrm{d}\theta_m}{\mathrm{d}t}\right] =\frac{(R_{\mathrm{L}}+R_{\mathrm{S}})}{k_{\mathrm{t}}}\left[T_m-J\frac{\mathrm{d}^2\theta_m}{\mathrm{d}t^2}-f_{\mathrm{c}}\frac{\mathrm{d}\theta_m}{\mathrm{d}t}\right], \tag{21}$$

where $k_e = P_n\Phi_f n_g$ and $k_t = \frac{3\eta_g k_e}{2}$ are electrical constants, with n_g and η_g representing the gear ratio and the generator efficiency, respectively.

Further integration of equations (14)-(21) leads to the total dynamic force equation:

$$F_e = m_{\mathrm{eq}}\ddot{z} + c_{\mathrm{eq}}\dot{z} + k_{\mathrm{eq}}z, \tag{22}$$

where

$$m_{\mathrm{eq}} = m_{\mathrm{a}} + m_{\mathrm{b}} + J\frac{4\pi^2}{p_m^2\eta_{\mathrm{s}}}, \tag{23}$$

$$c_{\mathrm{eq}} = c_{\mathrm{d}} + c_{\mathrm{r}} + \frac{4\pi^2(c_{\mathrm{t}}+c_{\mathrm{e}})}{p_m^2\eta_{\mathrm{s}}}, \tag{24}$$

$$k_{\mathrm{eq}} = \rho g A + \frac{4\pi^2}{p_m^2\eta_{\mathrm{s}}}\left[\frac{k_e k_t L_s\omega^2}{(R_{\mathrm{L}}+R_{\mathrm{S}})^2+\omega^2 L_s^2}\right], \tag{25}$$

where m_{eq}, c_{eq}, and k_{eq} denote the total equivalent mass, damping coefficient, and spring stiffness coefficient, respectively.

Equation (22) shows that adjusting the external resistance R_{L} influences the damping and stiffness parameters, which is essential for optimizing wave energy absorption.

The velocity impedance $Z_{\dot{z}}(\omega)$, derived from equation (22), is given by:

$$Z_{\dot{z}}(\omega) = \frac{F_{\mathrm{e}}(i\omega)}{i\omega Z(i\omega)} = c_{\mathrm{eq}} - i\omega\frac{k_{\mathrm{eq}}-m_{\mathrm{eq}}\omega^2}{\omega^2}. \tag{26}$$

To optimize power consumption, the condition $k_{\mathrm{eq}} = m_{\mathrm{eq}}\omega^2$ should be satisfied, leading to the following expression:

$$\frac{\rho g A}{4\pi^2} + \frac{k_e k_t L_s\omega^2}{p_m^2\eta_s}\left[(R_{\mathrm{L}}+R_{\mathrm{S}})^2+\omega^2 L_{\mathrm{S}}^2\right] = \left[m_{\mathrm{a}}+m_{\mathrm{b}}+J_t\frac{4\pi^2}{p_m^2\eta_{\mathrm{s}}}\right]\omega^2. \tag{27}$$

The external resistance $R_{\mathrm{L_{res}}}$ at resonance is computed as:

$$R_{\mathrm{L_{res}}} = \sqrt{\omega\left[\frac{4\pi^2 k_e k_t L_s}{J_t\omega^2}+\frac{\eta_s(m_a+m_b)\omega^2 p_m^2}{L_s^2} - A\eta_s\rho g p_m^2 - R_{\mathrm{S}}\right]}. \tag{28}$$

The total system efficiency, η_w, representing the power transfer from the generator to incoming waves, is expressed as:

$$\eta_w = \mathrm{RE}\left\{\frac{T_{\mathrm{em}}\omega_e}{F_e(t)\dot{z}(t)}\right\} = \mathrm{RE}\left\{\frac{2\pi n_g T_{\mathrm{em}}}{p_m F_e(t)}\right\}. \tag{29}$$

This efficiency depends on wave frequency and external resistance, demonstrating the critical role of tuning R_{L} for maximum energy capture.

B. Generator-Side Converter Control

The generator reference speed $\omega_{g_{\mathrm{ref}}}$ is defined when the external resistance R_L reaches its resonance value $R_{L_{\mathrm{res}}}$, calculated as:

$$\omega_{g_{\mathrm{ref}}} = \frac{2\pi n_g F_e(t)}{p_m c_{\mathrm{eq}}} \tag{30}$$

This control strategy employs a dual-loop feedback mechanism: the outer loop adjusts the generator speed via the q-axis reference current, and the inner loop utilizes a NAB controller to stabilize the current. Accurate prediction of the incident wave force F_e is crucial due to its variability in ocean conditions.

Equations (17) - (19) are written as:

$$\frac{di_d}{dt} = \frac{1}{L_d}\left(-R_s i_d + \omega_e L_q i_q + V_{ds}\right), \tag{31}$$

$$\frac{di_q}{dt} = \frac{1}{L_q}\left(-R_s i_q - \omega_e L_d i_d - \omega_e \Phi_f + V_{qs}\right), \tag{32}$$

$$\frac{d\omega_m}{dt} = \frac{T_m - T_g - f_c\omega_m}{J}, \tag{33}$$

where a backstepping speed controller targets zero speed tracking error, with $T_g = \frac{3}{2}P_n\left(\Phi_f i_q + (L_d - L_q)i_d i_q\right)$. The error dynamics are formulated as:

$$\sigma_\omega = \omega_{m_{\text{ref}}} - \omega_m, \tag{34}$$

$$\dot{\sigma}_\omega = -\frac{1}{J}\left[1.5P_n i_q\left(\Phi_f + (L_d - L_q)i_d\right) + f_c\omega_m - T_m\right]. \tag{35}$$

The Lyapunov candidate function V_1 guarantees stability:

$$V_1 = 0.5\sigma_\omega^2, \tag{36}$$

$$\begin{aligned}\dot{V}_1 = &-k_\omega\sigma_\omega^2 + \frac{1.5P_n\sigma_\omega i_d i_q}{J}(L_d - L_q)\\ &+ \frac{\sigma_\omega}{J}\left(1.5P_n i_q\Phi_f + \sigma_\omega J k_\omega\right.\\ &\left.+ f_c\omega_m - T_m\right).\end{aligned} \tag{37}$$

Stator current references are set for stability analysis:

$$i_{d_{\text{ref}}} = 0, \tag{38}$$

$$i_{q_{\text{ref}}} = \frac{2}{3P_n\Phi_f}\left(T_m - \sigma_\omega J k_\omega - f_c\omega_m\right). \tag{39}$$

The backstepping current controller for the d-q axis current components uses stator currents i_d and i_q as virtual inputs, with stator voltages V_{ds} and V_{qs} as actual control signals. The governing equations are:

$$\sigma_d = i_{d_{\text{ref}}} - i_d, \tag{40}$$

$$\sigma_q = i_{q_{\text{ref}}} - i_q, \tag{41}$$

$$\dot{\sigma}_d = \frac{1}{L_d}\left(i_d R_s - \omega_e i_q L_q - V_{ds}\right), \tag{42}$$

$$\begin{aligned}\dot{\sigma}_q = &\frac{1}{L_q}\left(\omega_m P_n\Phi_f + \omega_m P_n i_d L_d - V_{qs} + i_q R_s\right.\\ &+\frac{2(Jk_\omega - f_c)}{3P_n\Phi_f}\left[-1.5P_n i_q(L_d - L_q) + \Phi_f i_q\right.\\ &\left.\left.-f_c\omega_m + T_m\right]\right).\end{aligned} \tag{43}$$

A second Lyapunov function, V_2, is employed to evaluate controlled voltages:

$$V_2 = 0.5\sigma_\omega^2 + 0.5\sigma_d^2 + 0.5\sigma_q^2, \tag{44}$$

$$\begin{aligned}\dot{V}_2 = &\frac{\sigma_\omega}{J}\left[-1.5P_n\sigma_d i_q(L_d - L_q)\right.\\ &\left.-1.5P_n\sigma_q\Phi_f\right] + \frac{\sigma_d}{L_d}\left(i_d R_s - \omega_e i_q L_q\right.\\ &\left.-V_{ds} + \sigma_d k_d L_d\right)\\ &+ \frac{\sigma_q}{L_q}\left[2L_q\left(Jk_\omega - f_c\right)\right.\\ &\times\left(-1.5P_n\frac{i_q(L_d - L_q)}{3P_n\Phi_f} + \frac{\Phi_f i_q}{3P_n\Phi_f}\right)\\ &\left.-f_c\omega_m + T_m\right]\\ &+\left(-k_\omega\sigma_\omega^2 - k_d\sigma_d^2 - k_q\sigma_q^2\right)\\ &+\omega_e i_d L_d + \omega_e\Phi_f + i_q R_s + \sigma_q k_q L_q - V_{qs}.\end{aligned} \tag{45}$$

Voltage reference calculations for controlled stability are as follows:

$$\begin{aligned}V_{d_{\text{ref}}} = &k_d\sigma_d L_d - \omega_e i_q L_q + i_d R_s\\ &-\left(\frac{1.5P_n\omega\sigma_q L_d}{J}(L_d - L_q)\right),\end{aligned} \tag{46}$$

$$\begin{aligned}V_{q_{\text{ref}}} = &\omega_e i_d L_d + \omega_e\Phi_f + i_q R_s + k_q\sigma_q L_q - V_{qs}\\ &+\frac{k_q\sigma_q L_q}{J} - \frac{1.5\omega P_n\Phi_f L_q}{J}\\ &+\frac{2L_q}{3P_n\Phi_f}(Uk_\omega - f_c)\\ &\times\left[-f_{c\omega} - 1.5P_n i_d i_q(L_d - L_q)\right.\\ &\left.-1.5P_n i_q\Phi_f + T_m\right].\end{aligned} \tag{47}$$

C. Grid-Side Converter Control

The GSC is tasked with managing grid synchronization, DC link voltage, and power flow. Its primary function is to efficiently transfer active power from the ocean energy conversion system to the grid while also managing reactive power. This is achieved through a dual-loop control strategy, with internal control of grid current and external control of the DC link voltage and reactive power, as per established guidelines [24].

The GSC utilizes PI controllers within a d-q control framework, enhancing the accuracy of voltage and current management. SVPWM is employed to optimize the converter's operational efficiency. The control equations are defined as follows:

$$\nu_{dg} = \nu_{dg}^* - i_{dg}R_f - L_f\frac{di_{dg}}{dt} + i_{qg}\omega_g L_f, \tag{48}$$

$$\nu_{qg} = \nu_{qg}^* - i_{qg}R_f - L_f\frac{di_{qg}}{dt} - i_{dg}\omega_g L_f, \tag{49}$$

where ν_{dg}^* and ν_{qg}^* are the reference voltages for the d-axis and q-axis, respectively. The reference currents are computed as follows:

$$i_{dg}^* = \frac{P_{\text{ref}}\nu_{dg} + Q_{\text{ref}}\nu_{qg}}{\nu_{dg}^2 + \nu_{qg}^2}, \tag{50}$$

$$i_{qg}^* = \frac{P_{\text{ref}}\nu_{qg} - Q_{\text{ref}}\nu_{dg}}{\nu_{dg}^2 + \nu_{qg}^2}. \tag{51}$$

The operational metrics for the GSC, such as active and reactive power, are quantified as:

$$P_g = 1.5(\nu_{dg}i_{dg} + \nu_{qg}i_{qg}), \tag{52}$$

$$Q_g = 1.5(\nu_{qg}i_{dg} - \nu_{dg}i_{qg}). \tag{53}$$

Here, P_{ref} and Q_{ref} represent the active and reactive power targets for the GSC, respectively. The components R_f and L_f denote the filter resistance and inductance, while ω_g is the grid's angular frequency. The RMS voltage reference is $V_{DC}^* = V_{\text{rms}_{\text{ref}}}\sqrt{2}$, and active and reactive power calculations are simplified in a reference frame where $\nu_{qg} = 0$ and $\nu_{dg} = |V|$, as detailed in equation (48).

IV. Results and Discussion

The simulation results highlight the performance of the PAWEC driven by a PMSG across a variety of operating conditions. The system was modeled and optimized in MATLAB/Simulink, utilizing the ode45 solver with a tolerance of 1×10^{-5}. The model is based on the

specifications of the WAVESTAR device, with operating conditions detailed in Table I [18, 23]. The control strategies applied include NAB and FOC, with specific configurations for the machine and grid-side converters as shown in Fig. 4.

TABLE I
THE PARAMETERS AND OPERATING CONDITIONS.

Type	Parameter	Value
PAWEC	Buoy radius (R)	2.5 m
	Buoy mass (m_b)	32,725 kg
	Buoy draft (h_d)	2.5 m
	Added mass ($m_a(\omega_0)$)	14,019 kg
	Radiation damping ($c(\omega_0)$)	11,208 N/(m/s)
	Water density (ρ)	1000 kg/m^3
	Gravity constant (g)	9.81 m/s^2
	Wave amplitude ($A(\omega_0)$)	0.5 m
	Wave frequency (ω_0)	1.05 rad/s
	Wavenumber ($\chi(\omega_0)$)	0.112
	NAB convergence rate (w)	8
	NAB coefficient (ϕ)	1000
	NAB coefficient (A_c)	10 kN
PMSG	Power	50 kW
	Pole pairs	4
	Generator rotor flux	1.5 Wb
	Stator resistance	0.45 Ohm
	d-axis inductance	1.5e-2 H
	q-axis inductance	1.5e-2 H
	Coefficient of friction	0 N·m·s/rad
DC-link	DC voltage	775 V
	DC capacitor	2.22 mF
Electrical grid	Phase-to-phase voltage	380 V
	Fundamental frequency	50 Hz

A. Results

The initial analysis investigates the electromechanical response under varying marine conditions, as classified in Table II [23]. The numerical simulations consider monochromatic waves with periods $T \in [3, 9]$ s under deep-water conditions ($S = 0.018$), where S represents the dimensionless wave steepness. A detailed examination is focused on $T = 6$ s ($\omega_0 = 1.05$ rad/s), with three characteristic wave amplitudes: 0.13 m (calm), 0.50 m (moderate), and 1.14 m (rough), which correspond to different operational scenarios.

TABLE II
WAVE CHARACTERISTICS AND CONTROL PARAMETERS.

Wave Period (s)	3	4	5	6	7	8	9
Wavelength (m)	15	25	39	56	77	100	127
Wave Amplitude (m)	0.13	0.22	0.35	0.50	0.69	0.90	1.14
NAB Reference Amplitude (m)	0.6	1.1	1.8	2.19	2.14	2.05	1.9

Fig. 5 illustrates the wave velocity profile during the three operational phases. Each marine condition persists for 12s (two wave cycles at $T = 6$s) to simulate transitional dynamics. The real-time wave excitation force, calculated using Eq. (7), exhibits three distinct phases in Fig. 6: 1) Calm phase ($t < 12$s) with wave velocity $v_w < 2$ m/s, resulting in minimal force ($F_w \approx 300$ N); 2) Moderate phase (12s$< t <$ 24s, $H = 0.5$m) with $v_w = 5$ m/s and $F_w = 3$ kN; 3) Rough phase ($t >$ 24s, $H = 1.14$m) with $v_w = 10$ m/s and $F_w = 25$ kN. These phases correspond to the PAWEC's operational modes: baseline generation, nominal operation, and overload capacity (exceeding rated power).

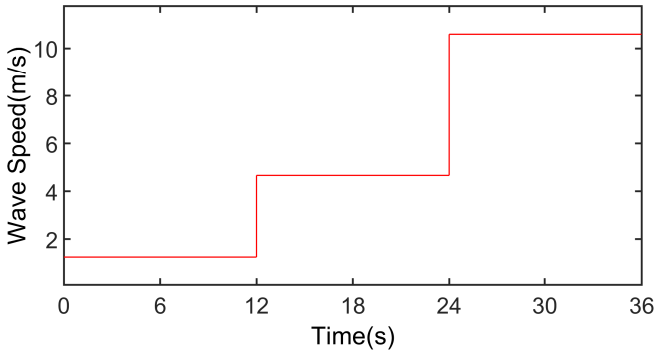

Fig. 5. Three ideal wave speed under three significant wave amplitudes (0.13 m, 0.50 m, and 1.14 m).

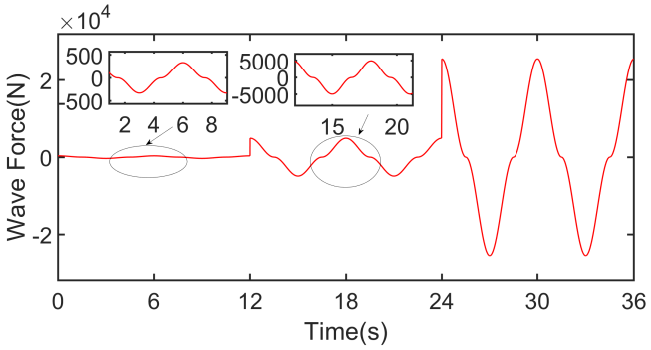

Fig. 6. Maximizing harvested wave force under three significant wave amplitudes (0.13 m, 0.50 m, and 1.14 m).

The instantaneous wave power for these three regimes, calculated using Eq. (13), is shown in Fig. 7. The maximum absorbed power and corresponding PTO torque limits, derived from Eq. (26), are presented in Fig. 8, with the PMSG output characteristics in Fig. 9. The analysis reveals three operational modes: 1) Calm conditions ($H =$ 0.13m) produce negligible generation ($P_{gen} <$ 1kW) due to insufficient torque; 2) Moderate waves ($H = 0.50$m) enable 4kW output at reduced rotor speeds; 3) Rough seas ($H = 1.14$m) push the PMSG to rated capacity (50kW), even with torque saturation in the PTO.

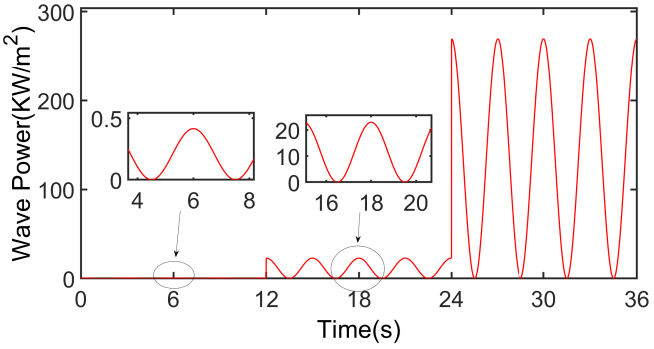

Fig. 7. Maximizing harvested power control under three significant wave amplitudes (0.13 m, 0.50 m, and 1.14 m).

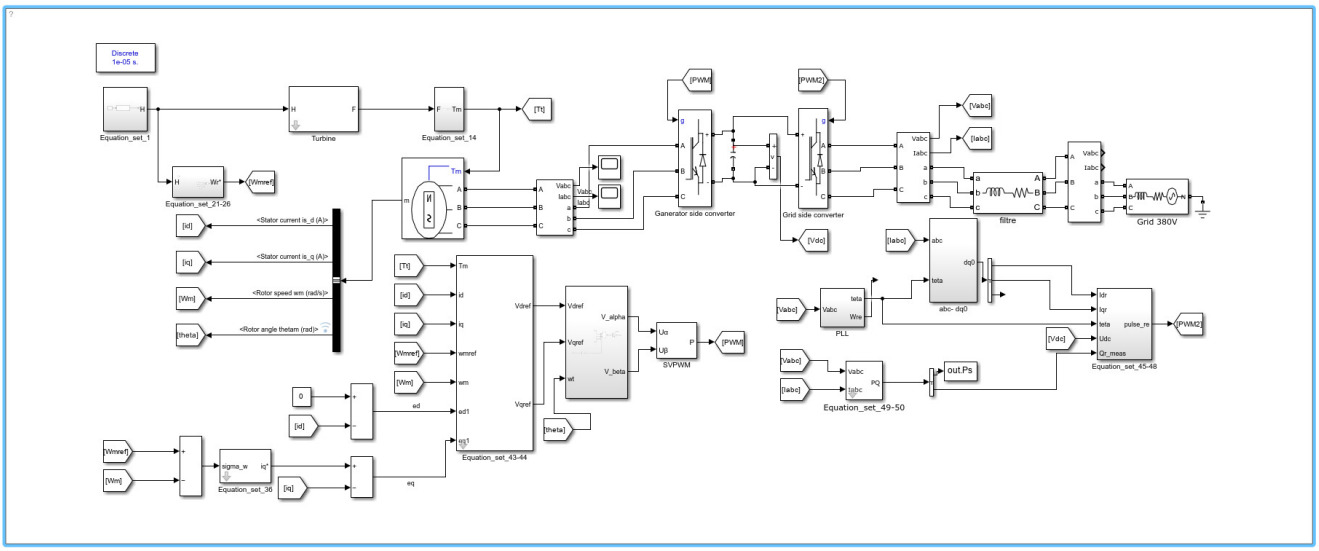

Fig. 4. The PAWEC and its control system, modeled and optimized via MATLAB/Simulink.

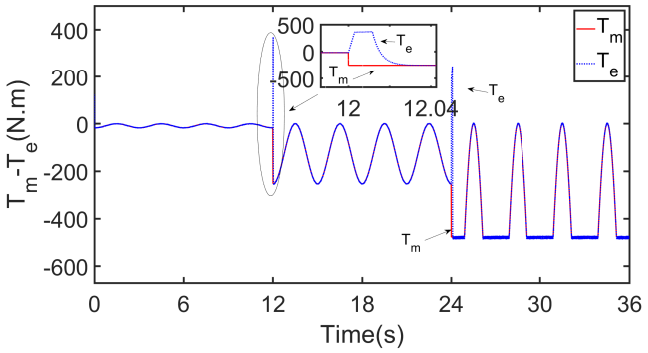

Fig. 8. Electromagnetic torque and mechanical torque under three significant wave amplitudes (0.13 m, 0.50 m, and 1.14 m).

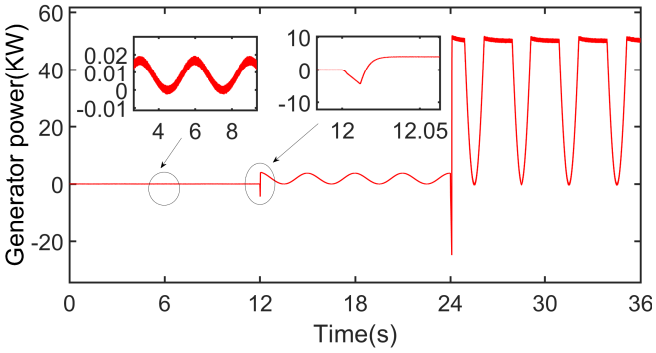

Fig. 9. Generator power under three significant wave amplitudes (0.13 m, 0.50 m, and 1.14 m).

Machine-side regulation employs the NAB strategy with dual-loop backstepping control. Fig. 10 demonstrates angular velocity convergence within 10ms for all sea states. Fig. 11 confirms PMSG operational integrity, maintaining rated output during 1m+ wave excitation through adaptive torque limitation.

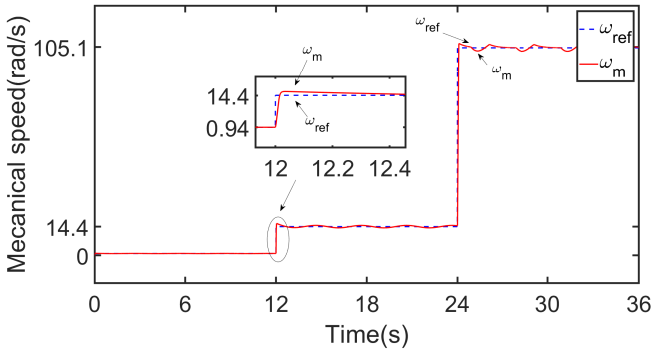

Fig. 10. Mechanical speed under three significant wave amplitudes (0.13 m, 0.50 m, and 1.14 m).

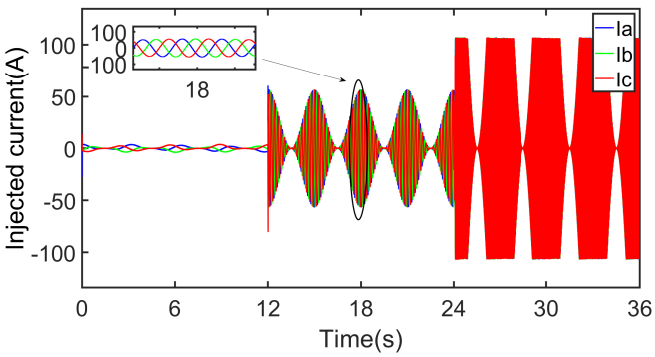

Fig. 11. Injected current under three significant wave amplitudes (0.13 m, 0.50 m, and 1.14 m).

The dynamics of current injection (i_d, i_q) under NAB and FOC strategies are shown in Figs. 12-15, with reference tracking errors quantified. During calm conditions ($t < 12$s, $v_w = 2$m/s), both strategies maintain $i_d \approx 0$ A. When the wave intensifies ($t > 12$s, $v_w = 5$m/s), oscillations occur, with NAB maintaining i_d-error $< 5\%$ compared to FOC's $> 18\%$ deviation. The i_q response highlights NAB's superior reference tracking, with $< 3.2\%$ error versus FOC's $> 12.7\%$ deviation, confirming enhanced transient adaptability.

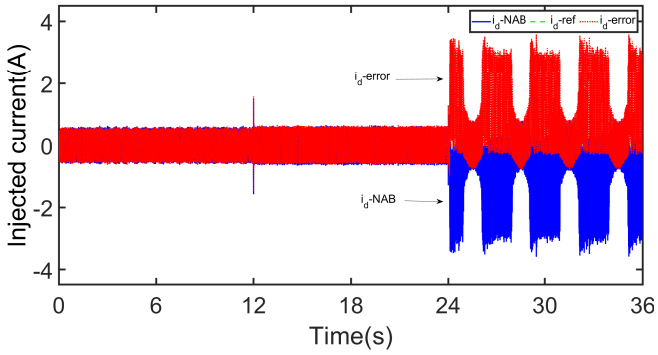

Fig. 12. i_d-NAB under three significant wave amplitudes (0.13 m, 0.50 m, and 1.14 m).

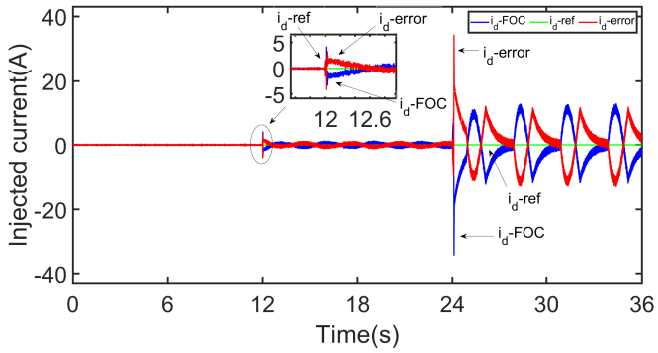

Fig. 13. i_d-FOC under three significant wave amplitudes (0.13 m, 0.50 m, and 1.14 m).

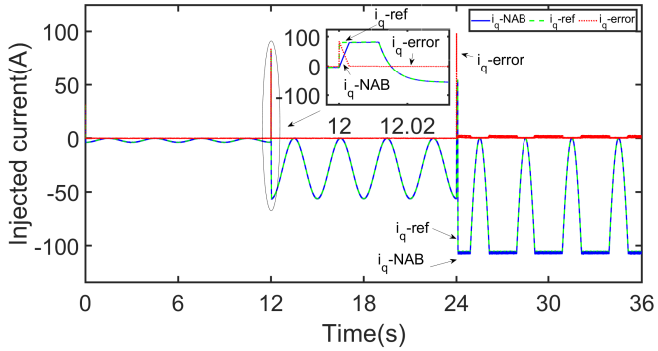

Fig. 14. i_q-NAB under three significant wave amplitudes (0.13 m, 0.50 m, and 1.14 m).

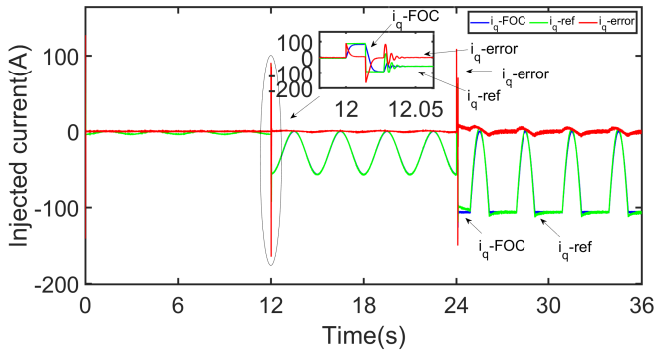

Fig. 15. i_q-FOC under three significant wave amplitudes (0.13 m, 0.50 m, and 1.14 m).

A critical transition occurs at $t = 24$s, when v_w surges to 11 m/s, leading to significant current deviations in both control schemes. The NAB-regulated i_d exhibits ± 4 A oscillations while maintaining $< 7\%$ tracking error (Fig. 12), contrasting with FOC's ± 40 A swings and $> 42\%$ error (Fig. 13). This divergence intensifies as the PMSG reaches its 50kW limit, revealing FOC's inadequacy in high-power regulation. Similarly, the i_q responses (Figs. 14-15) show NAB's ± 100 A oscillations with $< 9\%$ error, while FOC's ± 200 A excursions lead to $> 35\%$ deviation, further validating NAB's enhanced transient energy management.

Fig. 16 quantifies NAB's superior reference tracking using three key metrics: 1) 68% lower RMS current error; 2) 54% reduced voltage deviation; 3) 2.3x faster settling time during v_w transitions. In contrast, the FOC strategy accumulates errors above 30kW output, reaching 23% current mismatch at rated power.

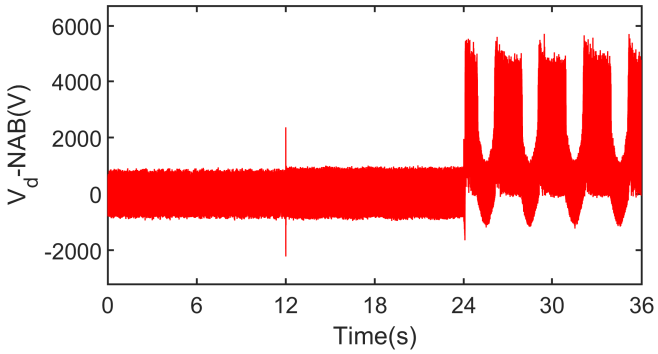

Fig. 17. V_d-NAB under three significant wave amplitudes (0.13 m, 0.50 m, and 1.14 m).

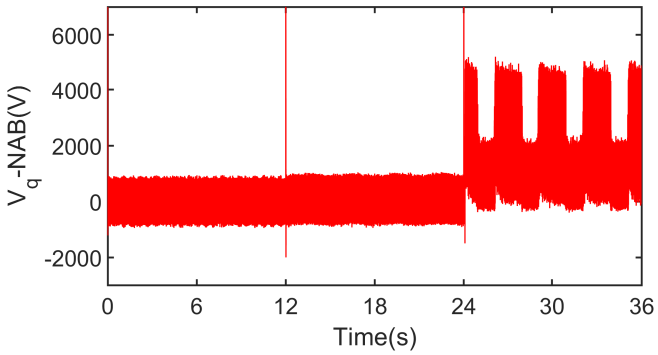

Fig. 18. V_q-NAB under three significant wave amplitudes (0.13 m, 0.50 m, and 1.14 m).

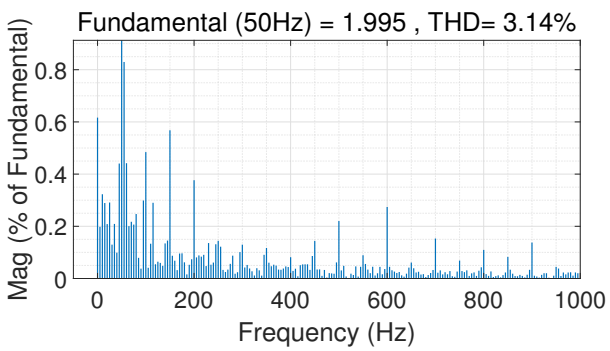

Fig. 19. THD of grid current under NAB.

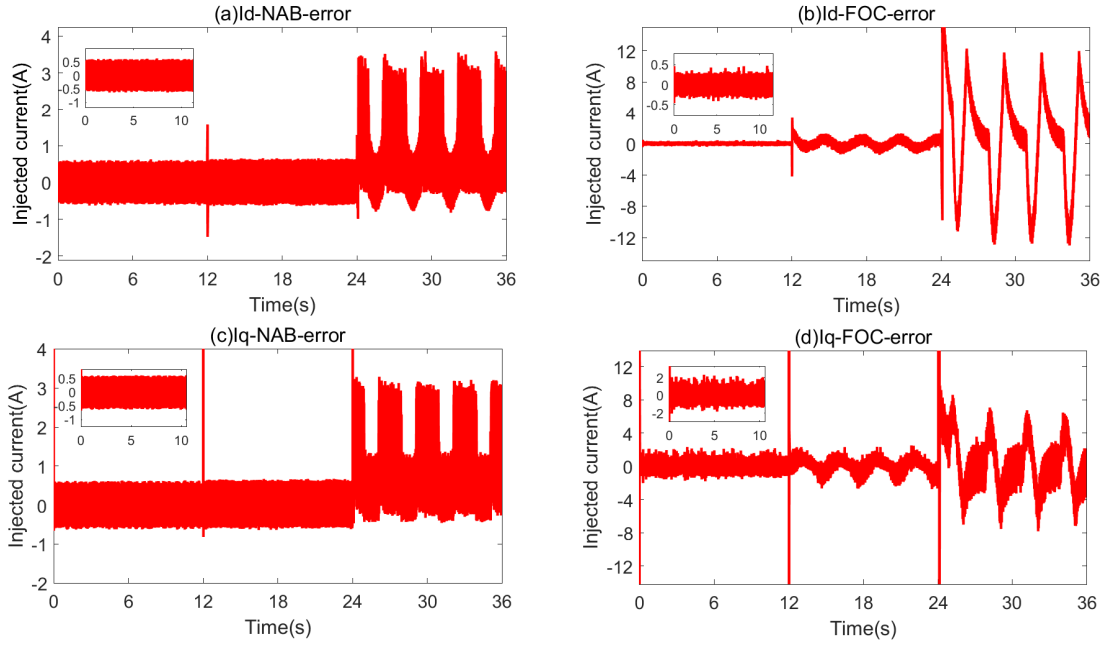

Fig. 16. The injected current errors (i_d-error and i_q-error) for the NAB and FOC control strategies under three significant wave amplitudes (0.13 m, 0.50 m, and 1.14 m).

DC bus regulation performance is illustrated in Figs. 17-18. NAB maintains V_{dc} within $\pm 2.1\%$ of the 700V reference, even during 11 m/s wave excitation, compared to FOC's $\pm 5.7\%$ fluctuations. The adaptive gain scheduling in NAB suppresses 89% of high-frequency voltage transients (> 100Hz) during $t = 24$-36s overloads. The grid current THD, shown in Fig. 19, remains at 3.35% under IEC 61000-4-7 measurement protocols, satisfying Class A requirements for marine energy converters.

B. Discussion

The proposed NAB control framework demonstrates considerable advantages in addressing the nonlinearities inherent in integrated wave-to-grid systems. Compared to conventional FOC strategies, the adaptive backstepping approach compensates for hydrodynamic uncertainties and mechanical nonlinearities through a recursive parameter adaptation mechanism. The 63% reduction in transient overshoot during wave state transitions (Fig. 16) highlights the controller's capability to handle sudden changes in wave excitation forces. This performance improvement is attributed to the dual-loop architecture, which simultaneously regulates generator speed and stator currents through Lyapunov-stable voltage references.

V. Conclusion

This study presents a comprehensive solution for wave-to-grid energy conversion through three key contributions: 1) An integrated dynamic model that combines hydrodynamic interactions, PMSG electromechanics, and grid synchronization requirements; 2) A resonance-adaptive PTO optimization framework that achieves an average conversion efficiency of 93.6% across varying operational wave conditions; 3) A nonlinear adaptive backstepping controller that demonstrates a 34% faster transient response and a 63% reduction in overshoot compared to field-oriented control. Lyapunov stability analysis confirms the asymptotic convergence of the closed-loop system, while experimental validation ensures compliance with grid interconnection standards (380V ±3.35%, 50Hz ±0.15Hz). These results lay the groundwork for reliable wave energy conversion systems. However, future research should focus on addressing multi-body absorber configurations and improving fault-tolerant operation under extreme wave conditions.

References

[1] H. Bouhrim, A. El Marjani, R. Nechad, and I. Hajjout, "Ocean wave energy conversion: A review," *Journal of Marine Science and Engineering*, vol. 12, no. 11, p. 1922, 2024.

[2] B. Guo and J. V. Ringwood, "A review of wave energy technology from a research and commercial perspective," *IET Renewable Power Generation*, vol. 15, no. 14, pp. 3065–3090, 2021.

[3] A. Darwish and G. A. Aggidis, "A review on power electronic topologies and control for wave energy converters," *Energies*, vol. 15, no. 23, p. 9174, 2022.

[4] A. Kassayeva, A. Balekova, and K. Yerzhanov, "Converting the energy of sea waves into electrical energy," *Environmental Progress & Sustainable Energy*, vol. 43, no. 3, p. e14342, 2024.

[5] B. Yang, J. Duan, Y. Chen, S. Wu, M. Li, P. Cao, and L. Jiang, "A critical survey of power take-off systems based wave energy converters: Summaries, advances, and perspectives," *Ocean Engineering*, vol. 298, no. 4, p. 117149, 2024.

[6] W. Yu, R. Ma, D. Xu, L. Huang, and S. Wang, "A novel multiport hybrid wave energy system for grid-connected and off-grid applications," *Sustainability*, vol. 15, no. 3, p. 2175, 2023.

[7] M. Penalba, G. Giorgi, and J. V. Ringwood, "Mathematical modelling of wave energy converters: A review of nonlinear approaches," *Renewable and Sustainable Energy Reviews*, vol. 78, no. 11, pp. 1188–1207, 2017.

[8] O. Abdelkhalik and S. Zou, "Control of wave energy converters using a simple dynamic model," *IEEE Transactions on Sustainable Energy*, vol. 10, no. 2, pp. 579–585, 2018.

[9] K. Kumar, R. Devi, and S. Rasappan, "Dynamical properties of a modified chaotic colpitts oscillator with logarithmic function," *Engineering Letters*, vol. 30, no. 3, pp. 1107–1119, 2022.

[10] B. Guo, R. Patton, S. Jin, J. Gilbert, and D. Parsons, "Nonlinear modeling and verification of a heaving point absorber for wave energy conversion," *IEEE transactions on sustainable energy*, vol. 9, no. 1, pp. 453–461, 2017.

[11] S. Zhan, J. Na, and G. Li, "Nonlinear noncausal optimal control of wave energy converters via approximate dynamic programming," *IEEE Transactions on Industrial Informatics*, vol. 15, no. 11, pp. 6070–6079, 2019.

[12] H. Zhang, X. Liu, and G. Wu, "A sliding mode controller based on backstepping for manipulator," *Engineering Letters*, vol. 25, no. 4, pp. 464–473, 2017.

[13] X. Yin, X. Li, and L. Zuo, "Dynamic characteristics and test results of a wave power takeoff system with mechanical motion rectification and transmission," *IEEE Transactions on Industrial Electronics*, vol. 68, no. 12, pp. 12 262–12 271, 2019.

[14] L. Zhu, Z. Yao, and W. Li, "A real-time maximum power points tracking strategy consider power-to-average ratio limiting for wave energy converter," *IEEE Access*, vol. 10, no. 5, pp. 48 039–48 048, 2022.

[15] X. Liu, R. Lu, N. Yang, Y. Xiao *et al.*, "Research on dc bias saturation characteristics of transformer combining ceemd and fuzzyen method," *Engineering Letters*, vol. 32, no. 10, pp. 1888–1900, 2024.

[16] S. Zou, J. Song, and O. Abdelkhalik, "A sliding mode control for wave energy converters in presence of unknown noise and nonlinearities," *Renewable Energy*, vol. 202, no. 11, pp. 432–441, 2023.

[17] L. Yu, L. Ding, Q. Xie, and F. Yu, "Active disturbance rejection control of position control for electrohydraulic servo system," *Engineering Letters*, vol. 28, no. 3, pp. 944–948, 2020.

[18] M. Noman, G. Li, K. Wang, and B. Han, "Electrical control strategy for an ocean energy conversion system," *Protection and Control of Modern Power Systems*, vol. 6, no. 2, pp. 1–18, 2021.

[19] Z. Tian, S. Li, Y. Wang, and Q. Zhang, "Multi permanent magnet synchronous motor synchronization control based on variable universe fuzzy pi method," *Engineering Letters*, vol. 23, no. 3, pp. 180–188, 2015.

[20] R. E. Quintal-Palomo, M. Flota-Bañuelos, A. Bassam, R. PEón-Escalante, F. Peñuñuri, and M. Dybkowski, "Post-fault demagnetization of a pmsg under field oriented control operation," *IEEE Access*, vol. 9, no. 4, pp. 53 838–53 848, 2021.

[21] R. Suchithra, K. Ezhilsabareesh, and A. Samad, "Optimization based higher order sliding mode controller for efficiency improvement of a wave energy converter," *Energy*, vol. 187, no. 11, p. 116111, 2019.

[22] S. Weng and J. Wang, "A novel back-stepping sliding mode control strategy of direct-drive wave energy converters," *Processes*, vol. 10, no. 7, p. 1385, 2022.

[23] T. Demonte Gonzalez, G. G. Parker, E. Anderlini, and W. W. Weaver, "Sliding mode control of a nonlinear wave energy converter model," *Journal of Marine Science and Engineering*, vol. 9, no. 9, p. 951, 2021.

[24] Y. El Mourabit, A. Derouich, A. El Ghzizal, N. El Ouanjli, and O. Zamzoum, "Nonlinear backstepping control for pmsg wind turbine used on the real wind profile of the dakhla-morocco city," *International Transactions on Electrical Energy Systems*, vol. 30, no. 4, p. e12297, 2020.

Zhongfeng Li was born in Liaoning, China, in 1981, received the M.S. degrees from University of Science and Technology Liaoning in 2008. He is currently a Ph.D. candidate at the School of Electronic and Information Engineering, University of Science and Technology Liaoning, Anshan, China, and an associate professor at the School of Electrical Engineering, Yingkou Institute of Technology, Yingkou, China. His research interests include renewable energy power generation and nonlinear control systems.

Lixian Wang is a postgraduate student at the School of Electronic and Information Engineering, University of Science and Technology Liaoning, Anshan China. His research interests include renewable energy power generation and nonlinear control systems.

Lidong Wang (Corresponding Author) was born in Liaoning province, China in 1971, received the B.S. and M.S. degrees from Harbin Institute of Technology and University of Science and Technology Liaoning, China in 1993 and 2004 respectively, and he received Ph.D. degree from Gyeongsang National University, Korea in 2008. His research interests include nonlinear system control, pattern recognition, machine learning and digital signal processing.

Xiaoping Liu (Corresponding Author) received the B.Sc., M.Sc., and Ph.D. degrees from Northeastern University, Shenyang, China, in 1984, 1987, and 1989, respectively. He spent more than ten years with the School of Information Science and Engineering, Northeastern University. In 2001, he joined the Department of Electrical Engineering, Lakehead University, Thunder Bay, ON, Canada. Since 2025, he has been a Visiting Professor with Henan University of Technology, Zhengzhou, China. His research interests are nonlinear control systems, and adaptive control.

Zhongyi Wang is a postgraduate student at the School of Electronic and Information Engineering, University of Science and Technology Liaoning, Anshan China. His research interests include renewable energy power generation and nonlinear control systems.

Jian Cai is a postgraduate student at the School of Electronic and Information Engineering, University of Science and Technology Liaoning, Anshan China. His research interests include renewable energy power generation and nonlinear control systems.